

Numerical Modelling of the Entrainment of Oxide Film Defects in Filling of Aluminium Alloy Castings

Xiaogang Yang^{1,*}, Xiaobing Huang², Xiaojun Dai³
John Campbell⁴, Joe Tatler¹

¹ASC Technology & Computer Science, North East Wales Institute of Higher Education,
Plas Coch Campus, Mold Road, Wrexham LL11 2AW, UK

²School of Engineering & Science, University of Paisley, Paisley PA1 2BE, UK

³IRC in Materials Processing, University of Birmingham, Edgbaston,
Birmingham B15 2TT, UK

⁴Department of Mechanical Engineering, University of Strathclyde, Glasgow G1 1XJ, UK

Abstract

Recent advances in understanding the filling process during casting have indicated that metal flow conditions play key roles in controlling the quality of the casting.^{2,15} Inappropriate filling of castings usually cause surface oxide films to be folded into the bulk liquid or broken due to a higher liquid metal kinematic energy, resulting in so-called “entrainment damage”. These folded oxide film defects are entrained in aluminium alloy casting and significantly affect both static and fatigue reliabilities.⁴

In the present study, an algorithm, Oxide Film Entrainment Tracking (OFET, 2-D), has been developed, tested, and validated for numerical modelling of the liquid aluminium flow and movement, fold-over and entrapment of oxide films during the mould filling process of aluminium castings. The Volume of Fluid (VOF) method is employed to track the free surface of liquid metal flow. A kinematic approach has been utilised for modelling the movement and entrainment of the oxide films on the liquid metal surface. Because the oxide films on the free surface are usually very thin, the inertial forces of the films can be disregarded in comparison to other forces like gravity and pressure. The computer program based on the proposed algorithm is able to model the metal flow behaviour and oxide film defect entrainment in filling of aluminium castings.

Keywords: Liquid metal flow, oxide film defects, numerical modelling, castings

*Author for all correspondence.

Tel: 01978-293090 Fax: 01978-293357 E-mail: x.yang@newi.ac.uk

Introduction

The effect of casting defects on the mechanical properties of aluminium castings has been investigated by a number of researchers, with the unanimous conclusion being reached, i.e. oxide films play a major role in the formation of these defects. Campbell² and Yang *et al.*¹⁵ demonstrated that improper design of the filling system usually results in an undesired higher metal flow velocity and surface turbulence so that the surface oxide films on the liquid aluminium advancing front is readily folded-over and entrapped into the bulk liquid metal. Since the oxide films (usually Al₂O₃ based) are actually solids, and very thin, the entrainment of the oxide films into the liquid metal flow in casting can be treated as a typical two-phase flow, with the densities of both phases being the same order. It was found that the entrapped oxide films are frequently accompanied by different casting defects such as shrinkage pore,¹ cracks and dross¹⁰ in solidified castings. Nyahumwa, Green and Campbell¹¹ found that young oxide films, old oxide films or a combination of both, initiated fatigue cracks when they studied the effect of surface turbulence on the fatigue strength of casting aluminium alloys. Caceres and Selling¹ indicated that the decrease in tensile properties of Al-Si-Mg cast aluminium alloys closely correlates with the area fraction of defects like porosity and oxide films in the fracture surface of the casting samples. Green and Campbell⁴ pointed out that the tangled networks of oxide films are actually cracks in the castings when they solidify, and the oxide film filling defects will significantly affect the strength distribution of castings.

The casting defects associated with oxide films in aluminium alloys may exhibit different morphologies such as “tangled or network”, “layer oxide or globular oxide”⁴ and “cloud or strip clustering particles”⁷. These oxide films originate from two main sources, (i) the melt preparation and (ii) the filling process. The former usually produces so-called “old” oxide films due to their formation over a long time.² These “old” oxide films may enter a mould accidentally and can be entrapped to form different type defects on solidification. A careful melt preparation and transfer can certainly avoid such defects to some extent, while the latter, the “young” oxide films, are formed as a result of the liquid aluminium stream transferring via the runner system to enter the mould cavity, taking place in a short time.² As indicated by Yang, Jolly and Campbell^{1,15} the “young” oxide films can be easily broken-up and incorporated into the liquid aluminium due to the surface turbulence, finally forming different defects in the castings. Because of the exposure time difference of these two types of oxide films, they will present different thickness in the filling.¹⁴ For example, the thickness of oxide

film measured on the liquid aluminium is 900nm at 700°C when the melt is held for 1 hour, and the measured oxide film thickness on 99.5% Al melt is about 24 nm after 5 seconds of exposure time at 700°C. It was also found that when the oxidation time was increased by a factor of ten, the oxide film thickness was doubled. Therefore, the “old” and “young” oxide films can be broadly identified by their thickness.

Defect-free castings are desirable because they will be reliable. The oxide film defects can be minimised if surface turbulence generated in filling is reduced.¹⁵ However, complete avoidance of surface turbulence during filling under gravity is impossible in reality. The number and size of the oxide films entrapped into the bulk liquid metal and their distribution in the castings are strongly associated with surface turbulence. It will be of significant practical value if the oxide film defects can be predicted. In their Flow-3D code, Flow Science Inc. has utilised a scalar variable concept to represent the likelihood of entrapped defects.⁸ In their oxide-tracking model, the scalar quantity accumulates at free surfaces at a constant rate. The scalar is treated to advect with the flow and a simple scalar transport equation is solved numerically. The scalar may be interpreted as proportional to the mass of contamination material per unit volume. Lin *et al.*⁹ proposed a numerical algorithm to simulate the movement, break-up and entrapment of oxide film inclusions encountered during the casting of aluminium alloys. However, quantitative validation of the predictions was not performed in their work due to lack of suitable experimental data. Zhao *et al.*¹⁶ proposed a semi-empirical algorithm to predict porosity distribution in castings with consideration of oxide entrapment during mould filling and hydrogen super saturation and volumetric shrinkage during solidification. Although these pioneer studies are useful to casting engineers, an algorithm that is capable of modelling of oxide film defect entrainment in casting is still sought.

The objective of this study is to propose and develop a 2-D algorithm *Oxide Film Entrainment Tracking* (OFET) for predicting such oxide film defect distribution during the filling. Although the “old” oxide films entering the mould are clearly an important source of defects in castings, this work focuses only on entrapped ‘young’ oxide films. The whole filling process, i.e. the flow of the melt through the channels that guides it into the mould cavity, during which young films are entrained, lasts only a few seconds. Numerical simulations of the oxide film defects in filling using the proposed algorithm has been compared with those attained using the commercial package, Flow-3D. Experimentally quantitative validation is also undertaken by the production of Al-7Si-Mg alloy castings, utilising light microscope and SEM techniques to

identify the microstructure of casting defects. The correlations between the defects, based on the SEM observation results, and the mechanical strength and reliability of the castings are compared with the numerical simulations.

Modelling of the oxide film entrainment

Liquid metal flow description and free surface tracking

The liquid metal flow during the filling is basically a transient free surface flow. Assuming the molten liquid metal flow to be incompressible, the governing equations with boundary conditions can be written as free surface evolution:

$$\frac{\partial F}{\partial t} + \nabla \cdot (\mathbf{u}F) = 0 \quad (1)$$

where F is the fractional volume-of-fluid contained in a computational cell, \mathbf{u} is the fluid velocity vector. This equation states that F moves with the liquid metal flow. Equation (1) has been employed in this investigation coupled with an oxide film entrainment-tracking algorithm as described below. When equation (1) is integrated over a computational cell, the change in F in a cell reduces to fluxes of F across the cell surfaces. The computation of fluxes is described in VOF method⁶ which uses a type of donor-acceptor flux approximation to avoid the smearing of the F function. The mass and momentum conservation in two-dimensional Cartesian coordinates can be expressed as

$$\nabla \cdot \mathbf{u} = 0 \quad (2)$$

$$\frac{\partial \mathbf{u}}{\partial t} + \nabla \cdot (\mathbf{u}\mathbf{u}) = -\frac{\nabla p}{\rho} + \nu \nabla^2 \mathbf{u} + \mathbf{f} \quad (3)$$

where p is the pressure and ρ is the density of the liquid metal, ν is the kinematic viscosity, and \mathbf{f} is the body force acting on the liquid metal. The pressure terms can be enclosed by the use of the Poisson equation, which combines the continuity and momentum equations and reads:

$$\frac{1}{\rho} \nabla^2 p = -\frac{\partial D}{\partial t} - \nabla \cdot [(\mathbf{u} \cdot \nabla)\mathbf{u}] + \nu \nabla^2 D \quad (4)$$

where D is the velocity divergence given by the left-hand side of equation (2). The reason for incorporating the Poisson equation for pressure is that there is the lack of a direct link for pressure between continuity and momentum equations.

The above transport equations are discretised using the finite different method. The transient terms are discretised using forward differencing, the convective terms are discretised using the first order upwind differencing while the pressure and diffusive terms are discretised using central differencing. The resulting linerised equations are solved using the Marker and Cell (MAC) method.⁵

Modelling of the movement of oxide films on free surface

A kinematic approach has been utilised for modelling the movement and entrainment of the oxide films on the liquid metal surface.³ Because the oxide films on the free surface are usually very thin, the inertial forces of the films can be disregarded in comparison to other forces like gravity and pressure. The Lagrangian equation describing the movement of oxide films can be written as:

$$\frac{d\bar{s}}{dt} = \bar{V} \quad (5)$$

where \bar{s} and \bar{V} are the displacement and velocity of a tracking point on the films, respectively. The velocities of the tracking points on the films can be determined by interpolating the velocities of the surrounding liquid metal. To ensure a proper determination of the positions of the films, sufficient tracking points are introduced. At time step n , the locations and the velocities of the tracking points can be obtained from the flow calculation. The positions of these points for next time step $n+1$ can be determined by the following equations:

$$\begin{aligned} x_i^{n+1} &= \text{MIN}\{x_i^n + 0.5(u_i^n + u_i^{n+1})\Delta t + CX, x_{is}^{n+1}\} \\ y_i^{n+1} &= \text{MIN}\{y_i^n + 0.5(v_i^n + v_i^{n+1})\Delta t + CY, y_{is}^{n+1}\} \end{aligned} \quad (6)$$

and where

$$\begin{aligned} CX &= \text{MAX}\{x_{is}^{n+1} - (x_i^n + 0.5(u_i^n + u_i^{n+1})\Delta t), 0.0\} \\ CY &= \text{MAX}\{y_{is}^{n+1} - (y_i^n + 0.5(v_i^n + v_i^{n+1})\Delta t), 0.0\} \end{aligned} \quad (7)$$

where x_{is}^{n+1} and y_{is}^{n+1} are the points which represent the liquid metal free surface as shown in Figure 1. The MIN feature in Eq. (7) prevents the displacement of the films out of the advancing free surface while the MAX feature readjusts those points back to the surface. In Figure 1, the points with the symbol “ \otimes ” which are joined by the dashed curve represent the positions of tracking points at time step $n+1$ without utilising the MIN and MAX features. The

solid curves with the symbols “①” and “②” indicate the liquid metal free surfaces obtained by the VOF method at time steps n and $n+1$.

The surface segments, which consist of the tracking points, are considered as film elements. In the simulation, a surface normal that is pointing away from the dryside of the surface element is introduced. If the local inertial pressure is larger than the restraining pressure, the oxide film will be torn but the film continuously reforms and repairs to allow the free surface to expand. A new tracking point is then added to account for the newly formed oxide film, which bridges the surrounding, track points. After new tracking points are added, all tracking points are renumbered. Theoretically, when the surface normals for the oxide film elements are pointing against each other, the oxide films, dry side to dry side, can be considered as entrained into the flow.² However, this actually imposes a barrier for numerical simulation. As can be seen from Figure 2, such oxide bifilms may fall into the same computational cell and the tracking points to characterise these films will be overlapped. Thus, it is necessary to remove some tracking points which fall into the same computational cell. In doing so, all the tracking points for the film elements have to be renumbered consecutively and a numerical algorithm to judge such fold over is proposed accordingly as described in Section 2.3. For the movement of films already entrapped in the liquid metal, the following equation is used.

$$\begin{aligned} x_i^{n+1} &= x_i^n + 0.5(u_i^n + u_i^{n+1})\Delta t \\ y_i^{n+1} &= y_i^n + 0.5(v_i^n + v_i^{n+1})\Delta t \end{aligned} \quad (8)$$

The treatment of films entrapped in the melt will be slightly different from treating those films on the free surface. It is assumed that once the oxide films are folded to be in contact, facing each other, there is no need to introduce new tracking points since no oxygen is available for the creation of more oxidised surface. This assumption neglects the real contribution that might be made by the air entrained between the double film, either trapped in macroscopic enclosed folds or bubbles, or as contained in the microscopic roughness of the oxide crystals.

Oxide film entrainment and fold over judgement - the numerical algorithm (OFET)

As shown in Figure 1, when the reflected liquid from the walls of the mould forms a backward rolling wave overlying the underneath stream, the oxide films are folded into the liquid metal, dry side to dry side. A careful observation of this phenomenon reveals that the velocities for

these two overlaid opposite flowing streams are always opposite. This information can be used to judge whether or not the oxide films are entrained and folded. Suppose that the fold over has taken place as shown in Figure 2. The velocities at both the top and bottom of the computational cell are employed.

$$F_{oxide} = \text{sgn} \left[\min \left(\frac{u_{i+\frac{1}{2},j+1}}{u_{i+\frac{1}{2},j}}, \frac{v_{i+\frac{1}{2},j+1}}{v_{i+\frac{1}{2},j}} \right) \right] \quad (9)$$

where $u_{i+\frac{1}{2},j}$ and $u_{i+\frac{1}{2},j+1}$ are the x-direction velocity components, and $v_{i+\frac{1}{2},j+1}$ and $v_{i+\frac{1}{2},j}$ are the y-direction velocity components at the bottom and topsides of the cell. The sign function, sgn , determines the sign of the smaller ratio between the velocity components. If F_{oxide} is negative, an oxide film entrainment or fold-over is judged to occur. If F_{oxide} is positive, no oxide film fold-over happens. The above OFET algorithm is expected to predict qualitatively the distribution of oxide films in the casting.

Specification of tracking points

As described in section 2.2, an array of tracking points on the free surface of the liquid metal is defined at each time step to characterise the oxide films formed. However, suitable specification of the interval between every two adjacent tracking points will be a key for realising Lagrangian tracking. It has been suggested by Campbell² that the Weber number, defined as the ratio of inertia pressure, ρU^2 , to the pressure due to surface tension, can be used to characterise the flow conditions associated with generation of surface turbulence. The We number in the range 0.2-0.8 defines the maximum limit for metal flow which is free from surface turbulence in approximate agreement with the theoretical prediction of $We = 1.0$ for critical balance condition. This can be also used to determine the maximum permitted interval between two tracking points, which is given by

$$l_{assign} = \frac{[We]\gamma}{\rho U_{Cri}^2} \quad (10)$$

where $[We]$ is the Weber number for the critical balance condition. γ is surface tension. U_{Cri} is the critical velocity and l_{assign} is the interval between two tracking points. For liquid aluminium,

$\gamma = 0.9$ N/m and $U_{Cri} = 0.5$ m/s, which will give $l_{assign} = 1.44 \times 10^{-3}$ m. At each new time step $t + \delta t$, if the interval between any two adjacent points exceeds a pre-assigned value, i.e. $L > l_{assign}$, the oxide film break-up (i.e. surface expansion) takes place and a new tracking point is added between these two tracking points. When the free surface is folded together, oxide bifilms will be formed and the tracking points to characterise these films will overlap. In such circumstance, the distance between two tracking points is likely to be far smaller than the pre-assigned l_{assign} . Thus, it is necessary to remove some tracking points to keep Lagrangian tracking manageable.

Experimental and numerical validation

Castings and mechanical property trials

Because this investigation concerns the predictions of oxide film defect entrainment in filling of aluminium castings, ingate velocities have a significant influence on generation of surface turbulence and oxide film defect entrainment. A well-characterised benchmark casting experiment¹³ was chosen as shown in Figure 3, which consists of a pouring basin, a tapered sprue, a runner and a mould cavity. To achieve different ingate velocities, two different runner system designs, a Vortex-flow Runner (VR) and a Rectangular Runner (RR) were devised as shown in Figure 3. These allow for providing quite different flow conditions in the runner and different velocities through the ingate. The vortex-flow runner has been identified to effectively reduce surface turbulence while the rectangular runner usually provides the ingate velocity larger than the critical velocity of 0.5 m/s,¹² giving rise to serious surface turbulence. It should be noted that the only difference between the runner systems was the cross-sectional shapes of the runners; the cross sectional areas were the same. This arrangement allows for a direct comparison of the liquid metal flow behaviour and the performance of the castings acquired by using different runner systems.

Chemically bonded sand of fineness AFS 60 was used to make the mould. The binder was a two part mixture based on resin (urethane/phenolic, 0.6 wt% PEPSET 5230) and catalyst (isocyanate, 0.6 wt% PEPSET 5112). The mixing time to disperse the binder into the sand was about 3 minutes. The moulds were allowed to cure for about 10 minutes prior to stripping from the pattern. Commercial LM25 aluminium alloy (Al-7Si-0.4Mg) was used to make the castings. All the castings were poured at a temperature of 735-740°C. Four castings were poured, two for each system. After casting, all the samples were subjected to heat treatment at 540°C for 6 hours, water quench and precipitation treatment at 160°C for 4 hours.

The structure of the castings was examined on polished samples by optical microscope, and by scanning electron microscope (SEM). In order to correlate the mechanical properties of the castings to the defects observed, all the cast plates were machined to form 2×10 specimens as shown in Figure 4. These were subjected to a four-point bend test and consequently, the fractured smaller samples were then subjected to three-point bend test.

Numerical simulation

Based on previous work,¹⁵ the maximum flow velocity in the ingate is at the right-hand edge (the edge furthest from the down-sprue) for both the VR and RR runner at the moment when the liquid metal front enters the mould, with the value reaching 0.4 ms^{-1} and 0.7 ms^{-1} in the cases of VR and RR runners, respectively. In the case of VR runner system, the metal velocity entering the mould was maintained below 0.5 ms^{-1} for the entire filling time.

Numerical simulations of the filling processes for two cases, which employ different runners, are shown in Figure 5a, 5b. It can be seen from Figure 5a that the liquid metal flow for the ingate velocity 0.4 ms^{-1} (equivalent to the use VR runner system) is smooth, and neither splash nor folding-over of the melt can be observed when the liquid aluminium enters the mould cavities. In contrast to the case of 0.4 m/s , the liquid metal flow in the case of ingate velocity 0.7 ms^{-1} , using RR runner system, (Figure 5b) exhibits an undesirable behaviour: the melt fountains and folds over, thus giving rise to the possibility of generating oxide film defects. The predicted filling behaviour for the two cases using Flow-3D is shown in Figure 6. It can be seen from Figure 5 and Figure 6 that the predicted filling behaviour for both cases using the developed program and Flow-3D is in good agreement.

Corresponding to Figure 5, the predicted distributions of entrapped oxide films in the castings using the OFET numerical algorithm are shown in Figure 7a and 7b. It can be seen from Figure 7a that the predicted probability of oxide film defects is basically excluded from the internal zone of casting, and highest oxide film probability is distributed around the edge of the casting. This implies a better mechanical strength of the castings since the bend test assesses the central areas. Figure 7b clearly shows that the entrained oxide films are concentrated in the body of the castings. Similar results using Flow-3D are also obtained when the scalar variable is used to characterise the likelihood of oxide defects occurring in castings, as can be seen from Figure 8.

Experimental validation

An Omniment3 Instrument image analyser was used to observe the microstructure and to conduct quantitative analysis of the castings. The OMNIMET GPIA software was employed to analyse the acquired measurements. Image analysis of defects in aluminium castings was done based on the difference in the depth of view where the casting defects appear much darker than the surrounding phases, and therefore, can be confirmed on the basis of grey scale. The casting defect area and density were measured to characterise specific features. For each observation targeting on the field of a sample, the area fraction of the detected casting defects was obtained by dividing the detected defect areas by the area of the measurement field.

$$\alpha_F = \frac{\sum A_i}{A_T} \quad (11)$$

where α_i is the casting defect area fraction, A_i is the detected individual defect area and A_T is the area of measurement field. Similarly, the number of detected casting defects can be counted in each observation field, which is divided by the field area (mm^2) to define the casting defect density (numbers per unit area):

$$\rho_F = \frac{N_i}{A_T} \quad (12)$$

where ρ_F is the casting defect density, N_i is the number of detected casting defects. In the measurement, a contiguous measurement frames were used to calculate the casting defect density and area fraction of each sample. When counting the casting defects, care had to be taken to correct the edge effect so that those casting defects across the boundary of an observation field were counted once only.

The distributions of casting defect density for polished casting plate samples, acquired using VR and RR runners, are shown in Figure 9. Figure 10 illustrates the casting defect area fraction distributions for the two cases. It can be seen from Figures 9 and 10 that the quantities of both casting defect density and casting defect area fraction for the case using VR runner were uniformly distributed across the whole cast plate while these quantities for the case using RR runner were concentrated around the ingate. The ingate had a much higher defect density and area fraction. Direct comparison between the experimental measurements and numerical simulations indicated that the results of quantitative analysis of casting defect distribution were

still qualitatively consistent with the numerical simulation of oxide film defect distribution in the castings for both cases. It should be noted that the experimentally quantitative analysis of casting defects in this work accounts for all the casting defects, including gas pores, shrinkage pores and other oxide film defects that were found in the castings. Figure 11 shows the typical microstructures of various porosities in the polished surfaces of the samples taken from by optical microscope (Omniment3 Instrument Image Analyser). The porosities shown in Figure 11a are distributed independently and presented as in round shape while the porosities shown in Figure 11b are presented in cluster form, which the actual structure exists in castings as sketched in Figure 12. In general, the method employed in this study, which was based on the shape of pores, was able to discriminate between the two forms of porosity. However, such a distinction was not considered to be relevant because most porosity is in any case assumed to be closely related to the presence of oxide films.² The difficulty of differentiating accurately between these defects was therefore avoided. Furthermore, of course, the generation of gas or shrinkage porosity is dependant to great extent on metallurgical factors, and especially the solidification process. Such factors have not been included in the present modelling.

Discussion

The results for the case of ingate velocity of 0.7 m/s (the RR running system) are consistently poorer when judged by oxide film entrainment tracking simulation, casting defect density and casting defect area fraction distributions. This consistency strongly suggests that the castings filled with a higher ingate velocity, in particular greater than the critical velocity of 0.5 m/s,² are most likely defective. Indeed, it was observed from the simulations that when the ingate velocity is greater than 0.5 m/s, the melt certainly forms fountain and folds over, thus generating the surface turbulence. This could be especially important in the brief but vulnerable period when the runner is still priming and the melt is just entering the mould through the ingate, so that there is freedom for the melt to jump and splash, creating additional area for the creation of new films. The use of lower ingate velocity (the VR running system) showed that once the ingate velocity is less than the critical velocity of 0.5 m/s, the liquid metal fountaining, which may contribute to the generation of surface turbulence, could be avoided. This is the condition of the Weber number being smaller than unity. In order to convert the high velocity of the liquid metal at the exit of the sprue into a relatively gentle and smooth stream, advancing with a velocity less than the critical velocity for the entrainment of the surface as the metal enters the mould cavity, the filling system has to be effective in dissipating sufficient kinetic

energy of the liquid metal. The use of vortex flow runner (VR) provides a strong organisational movement of the liquid as it enters the runner via the sprue. The organised behaviour extends along the length of the runner, assisting the reduction of ingate velocity as a result of the considerable dissipation of energy by the rapid rotation.

The above results demonstrate the important role played by oxide films during the filling of the mould. The results confirm the expectations as indicated in the introduction, that the "young" oxide films are closely related to surface turbulence. Thus, a reduction in surface turbulence will reduce the possibilities of free surface break-up and the entrapment of surface oxide films. It seems that by optimising the runner system design and improving the flow behaviour during the filling, the fluid velocity in the ingate can be reduced to be less than the critical velocity 0.5 m/s^2 and the entrainment of "young" oxide films into the castings can be significantly reduced so that the mechanical strength and reliability of aluminium alloy castings can be enhanced.

The above results can be further justified by considering the correlation coefficient distribution as shown in Figures 13 and 14. The correlations between three-point bend strength (UBS) and casting defect density or area fraction are defined respectively by

$$R_{\rho_F-UBS} = \frac{[\sigma_{i,j}] \cdot \left[\frac{1}{\rho_F} \right]}{\left\{ [\sigma_{i,j}] \cdot \left[\frac{1}{\rho_F} \right] \right\}_{\max}} \quad (12)$$

$$R_{\alpha_F-UBS} = \frac{[\sigma_{i,j}] \cdot \left[\frac{1}{\alpha_F} \right]}{\left\{ [\sigma_{i,j}] \cdot \left[\frac{1}{\alpha_F} \right] \right\}_{\max}} \quad (13)$$

where R_{ρ_A-UBS} is the correlation coefficient between casting defect density and three-point bend strength (UBS) and R_{α_F-UBS} represents the correlation coefficient between casting defect area fraction and three-point bend strength (UBS). If the correlation coefficients R_{ρ_A-UBS} or R_{α_F-UBS} have the values close to 1, it means that casting defect distribution across the castings is more uniform with less concentrated defects. In contrast, a smaller correlation coefficient R_{ρ_A-UBS} or

$R_{\alpha F-UBS}$ indicates that there exist more concentrated casting defects. Obviously, higher correlation coefficients characterise more reliable castings. It can be seen from figures 13 and 14 that almost all the correlation coefficients $R_{\rho A-UBS}$ or $R_{\alpha F-UBS}$ are between 0.3 and 0.7 for the VR runner and from 0.11 to 0.80 for the RR runner.

Based on the above analysis, it seems that the mechanical strength properties of castings are determined not only by the number of casting defects in the castings but also determined by the features of casting defect fractions and the defect morphology. Concentrated casting defect distributions such as shrinkage porosity and casting defects with sharply notched shapes will cause local stress concentration, thus influencing the mechanical strengths.

Conclusions

A numerical algorithm, Oxide Film Entrainment Tracking (OFET, 2-D), for predicting the oxide film defects distribution in the liquid aluminium throughout the filling has been proposed and incorporated into the free surface tracking code developed for simulating filling. The results attained using the proposed numerical algorithm are in good agreement with those using the CFD code – Flow-3D and are qualitatively consistent with the experiments. It is found from numerical simulation that ingate velocities significantly affect the number and distribution of the oxide film defects generated from filling. The reduction of ingate velocity can effectively reduce casting defects. This can be achieved by controlling the chaotic behaviour of liquid metal flow and by the use of a vortex flow regime to dissipate the kinetic energy of the metal in the runner.

Acknowledgements

The authors wish to acknowledge the financial support of the EPSRC under the contract GR14507/01. The assistance of Mr. David Cloney, Mr. John Turner and Mr. Willie Logan of University of Paisley are appreciated.

References

1. C. H. Caceres and B. I. Selling, "Casting defects and the tensile properties of an Al-Si-Mg alloy", *Mater. Sci. Eng. A*, 1996, **220**, 109-116.
2. J. Campbell, *Castings 2nd Edition*, Butterworth-Heinemann, Oxford, UK, 2003.

3. X. Dai, X. Yang, J. Campbell & J. Wood, "The Influence of Oxide Film Defects generated in Filling on the Mechanical Strength of Aluminium alloy Castings", *Materials Science and Technology*, 2004, **20**(4), 505-513.
4. N. R. Green and J. Campbell, "Influence of oxide film filling defects on the strength of Al-7Si-Mg alloy castings", *AFS Transactions*, 1994, **102**, 341-347.
5. H. F. Harlow and E. J. Welch, "Numerical Calculation of Time-Dependent Viscous Incompressible Flow of Fluid with Free Surface", *Phys. Fluids*, 1965, **8**(12), 2183-2189.
6. C. W. Hirt and B. D. Nichols, "Volume of Fluid (VOF) Method for the Dynamics of Free Boundaries", *J. Comput. Phys.*, 1981, **39**, 201-225.
7. L. W. Huang, W. Shun & T. S. Shih, "Diagnosis and analysis of oxide film in Al-Si-Mg alloys", *AFS Transactions*, 2000, **108**, 547-560.
8. Flow-3D User's Manual Version 7.7. Flow Science Inc.
9. J. Lin, M. A. R. Sharif & J. L. Hill, "Numerical simulation of the movement, breakup and entrapment of oxide films during aluminium casting", *Aluminum Transactions*, 1999, **1**, 71-78.
10. M. Divandari "Mechanisms of Bubble Damage in Castings", PhD Thesis, University of Birmingham, 2001.
11. C. Nyahumwa, N. R. Green & J. Campbell, "Effect of mold filling turbulence on fatigue properties of casting aluminium alloys", *AFS Transactions*, 1998, **106**, 215-223.
12. J. Runyoro, S. M. A. Boutorabi & J. Campbell, "Critical gate velocities for film forming casting alloys: A basis for process specification", *AFS Transactions*, 1992, **100**, 225-234.
13. B. Sirrell, M. Holliday & J. Campbell, "Benchmark testing the flow and solidification modelling of Al castings", *JOM*. 1996, March 1996, 20-23.
14. W. G. Thiele, "Die oxidation von Aluminium und Aluminiumlegierungs Schmelzen", *Aluminium* 1962, **38**, 707-715.
15. X. Yang, M. Jolly & J. Campbell, "Minimization of surface turbulence during filling using a Vortex-flow runner", *Aluminum Transactions*, 2000, **2**, 67-80.
16. H. Zhao, I. Ohnaka, Y. Sako, H. Onda, J. Zhu & H. Yasuda, "Estimation of porosity defects with consideration of oxide entrapment", *Proceedings of the 65th World Foundry Congress* (Gyeongju, Korea), 2002, 749-754.

FIGURE CAPTIONS

Figure 1. Tracking points on the oxide film at time steps n and $n+1$, the oxide film points are located at the end of arrows.

Figure 2. A sketch of how to judge the oxide film fold over

Figure 3. Benchmark test casting moulds employing two different runner systems (a) Vortex-flow runner; (b) Rectangular runner; (c) offset step pouring basin.

Figure 4. Casting specimens (sampled from the VR cast plate), subjected to a four-point bend test (blue fracture line). The fractured smaller samples were subsequently subjected to a three-point bend test (red fracture lines).

Figure 5. Numerical simulations of filling processes of two different filling systems. (a) VR runner system; (b) RR runner system.

Figure 6. Numerical simulations of filling processes of two different filling systems using Flow-3D code. (a) VR runner system; (b) RR runner system.

Figure 7. Predicted susceptible oxide film defect distribution in the castings by using the OFET numerical algorithm. (a) VR runner system; (b) RR runner system.

Figure 8. The scalar variable distribution plots of two runner systems for (a) VR runner system; (b) RR runner system. Simulated by the FLOW-3D software.

Figure 9. The measured distributions of casting defect density (number per unit area) in casting plates. (a) RR runner; (b) VR runners.

Figure 10. The measured area fraction distribution of casting defects in casting plates. (a) RR runner; and (b) VR runner.

Figure 11. Typical microstructures of various porosities in polished surfaces of the samples, acquired by using optical microscope (from Omniment3 Instrument Image Analyser). (a) Porosity (b) Shrinkage porosities.

Figure 12. Schematic display of a shrinkage pore and the two-dimensional image acquired when the sample is sectioned.

Figure 13. The correlation coefficient distribution plots between casting defect density and three-point bend strength (UBS). (a) RR runner; (b) VR runner.

Figure 14. The correlation coefficient distribution plots between casting defect area fraction and three-point bend strength. (a) RR runner; (b) VR runner.

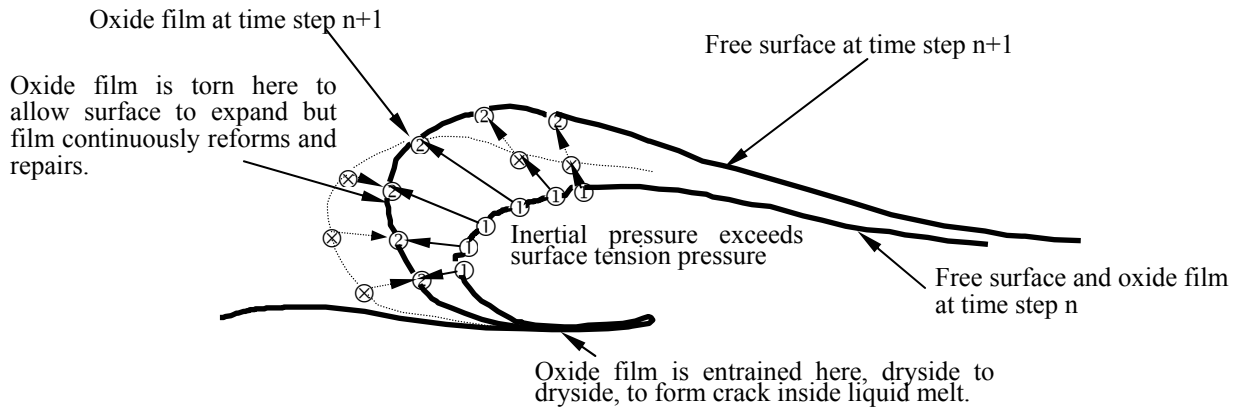


Figure 1. Tracking points on the oxide film at time steps n and n+1, the oxide film points are located at the end of arrows.

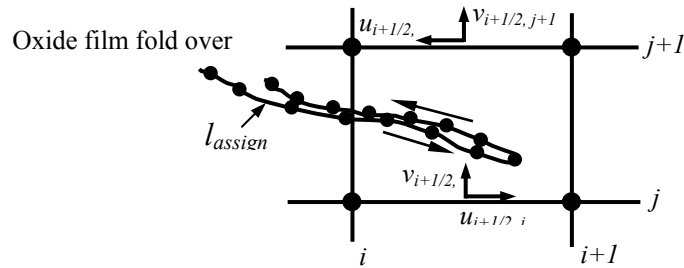


Figure 2. A sketch of how to judge the oxide film fold over

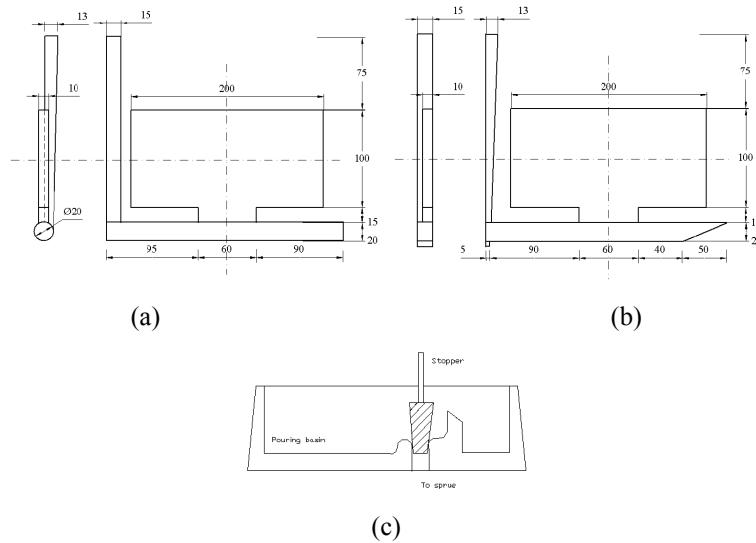


Figure 3. Benchmark test casting moulds employing two different runner systems (a) Vortex-flow runner; (b) Rectangular runner; (c) offset step pouring basin.

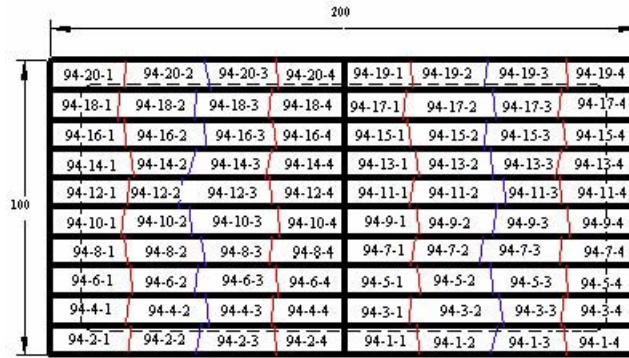


Figure 4. Casting specimens (sampled from the VR cast plate), subjected to a four-point bend test (blue fracture line). The fractured smaller samples were subsequently subjected to a three-point bend test (red fracture lines).

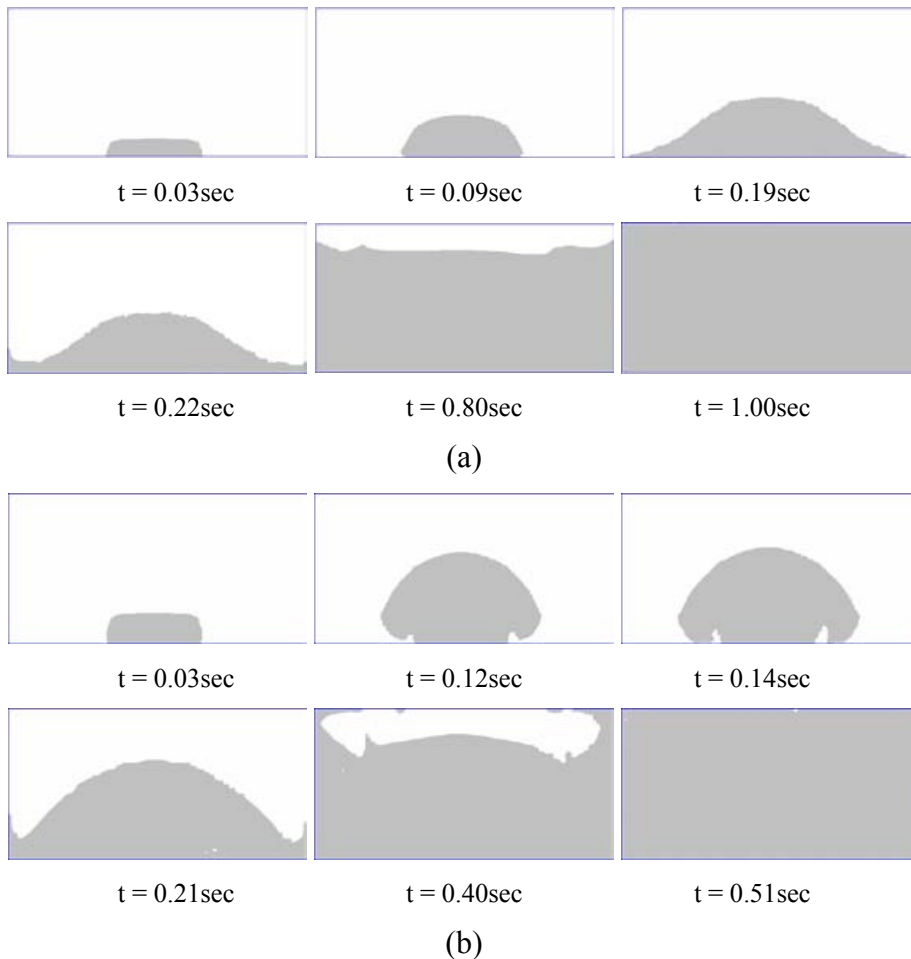


Figure 5. Numerical simulations of filling processes of two different filling systems. (a) VR runner system; (b) RR runner system.

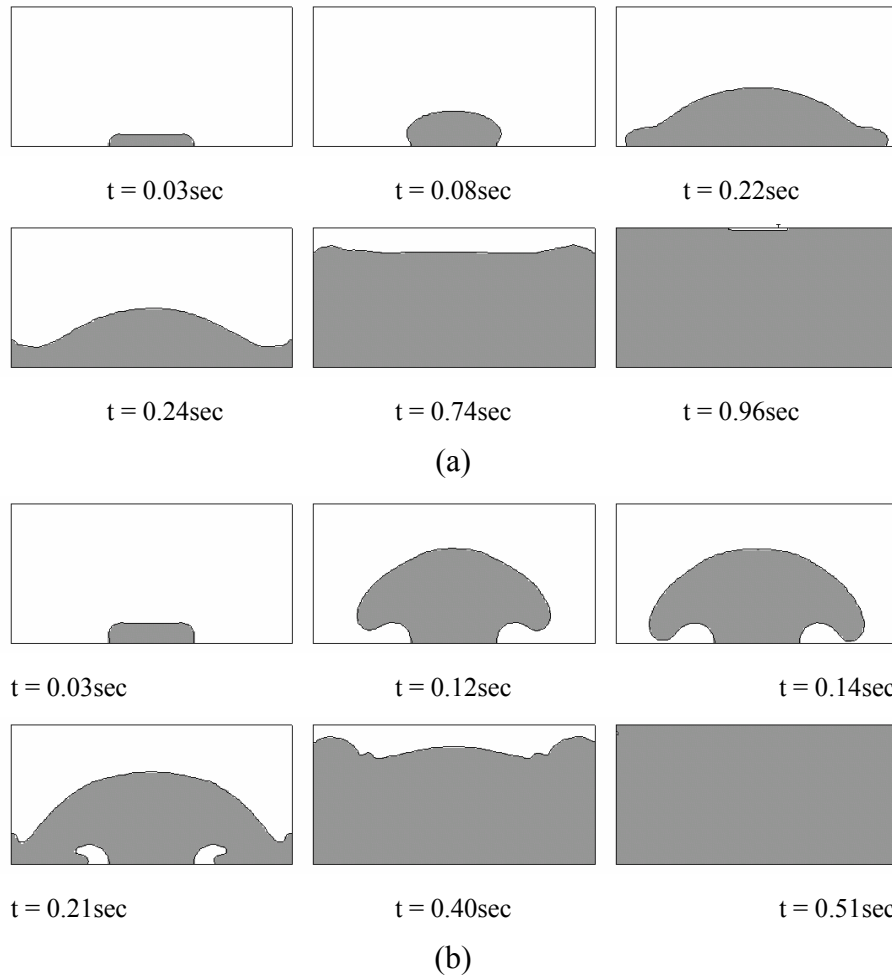


Figure 6. Numerical simulations of filling processes of two different filling systems using Flow-3D code. (a) VR runner system; (b) RR runner system.

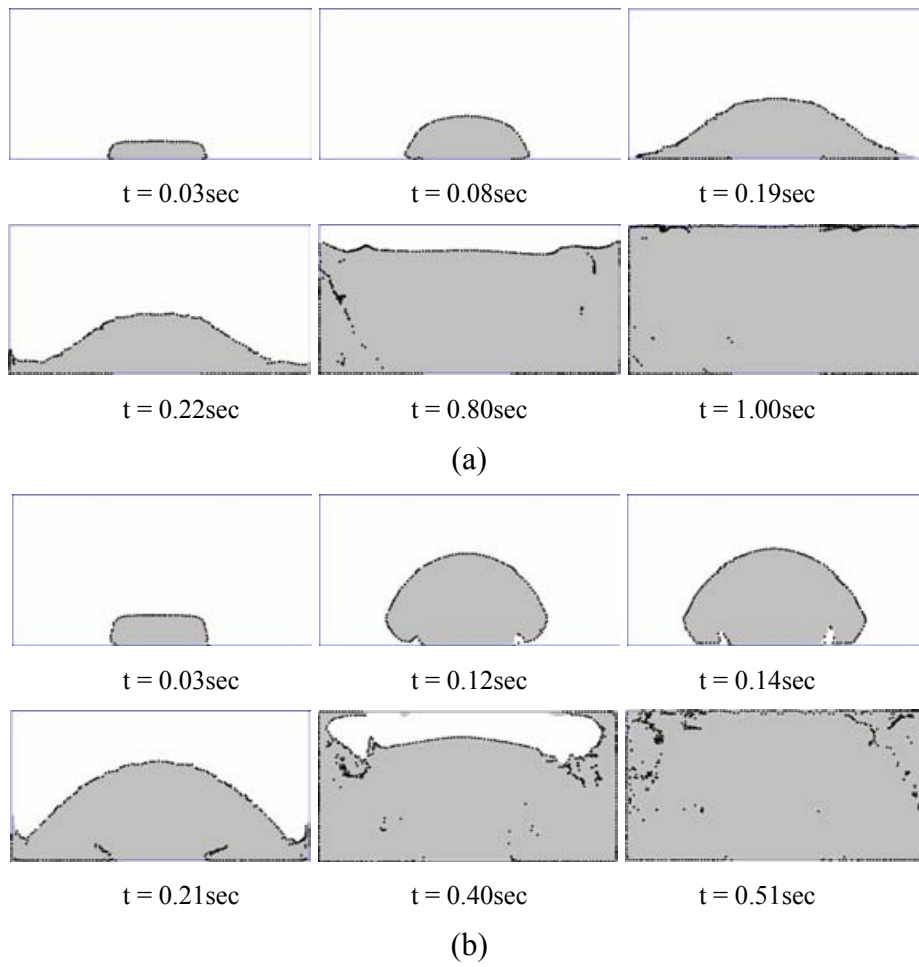


Figure 7. Predicted susceptible oxide film defect distribution in the castings by using the OFET numerical algorithm. (a) VR runner system; (b) RR runner system.

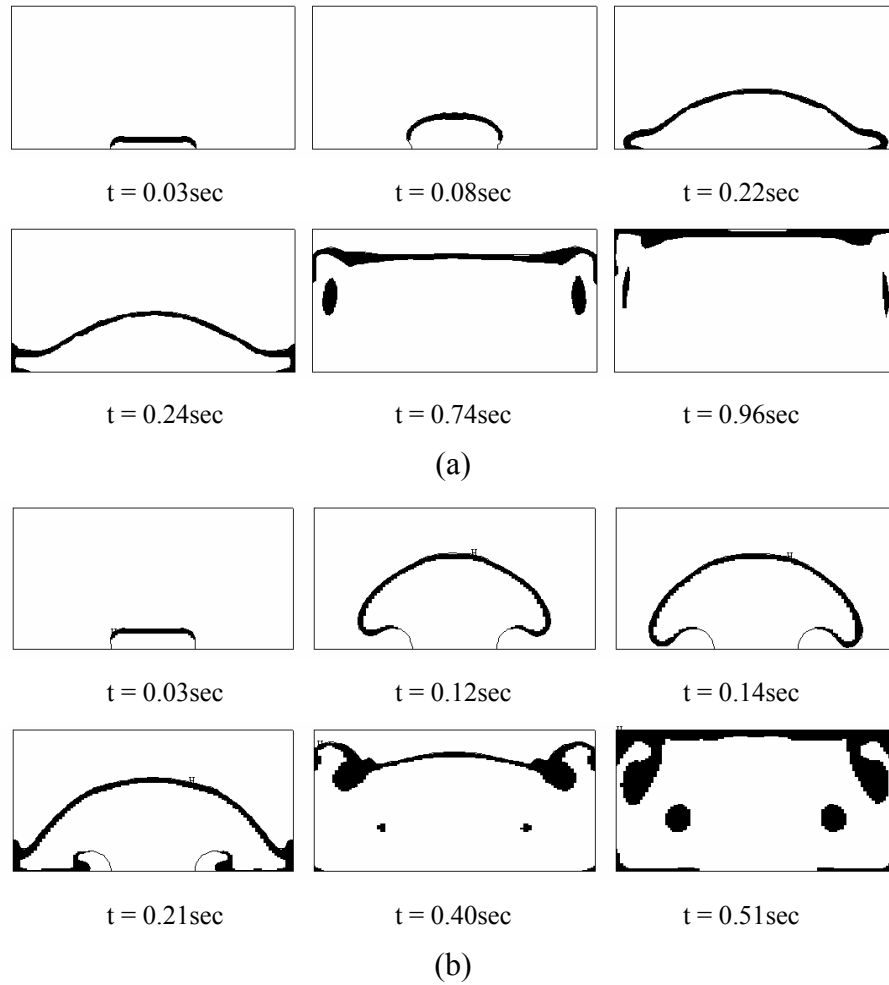
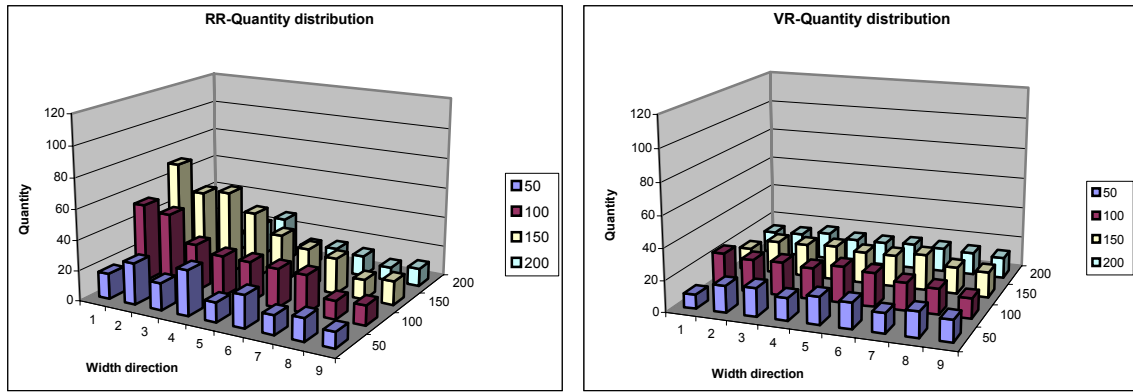


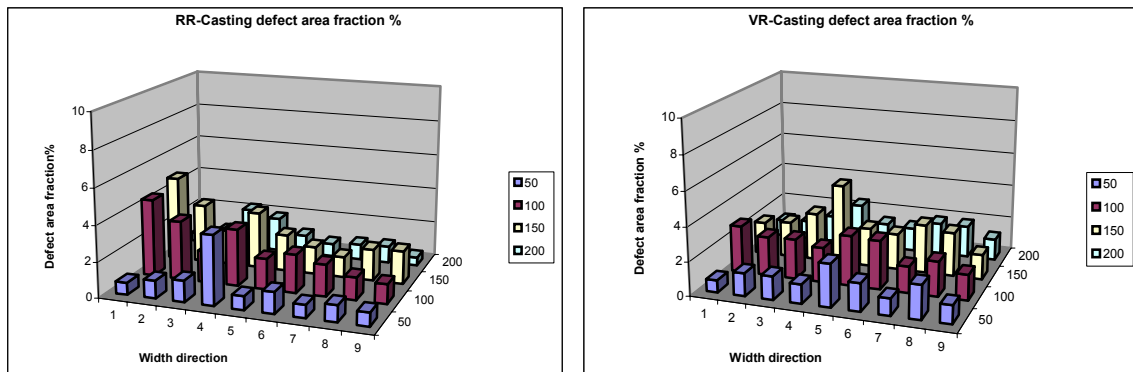
Figure 8. The scalar variable distribution plots of two runner systems for (a) VR runner system; (b) RR runner system. Simulated by the FLOW-3D software.



(a)

(b)

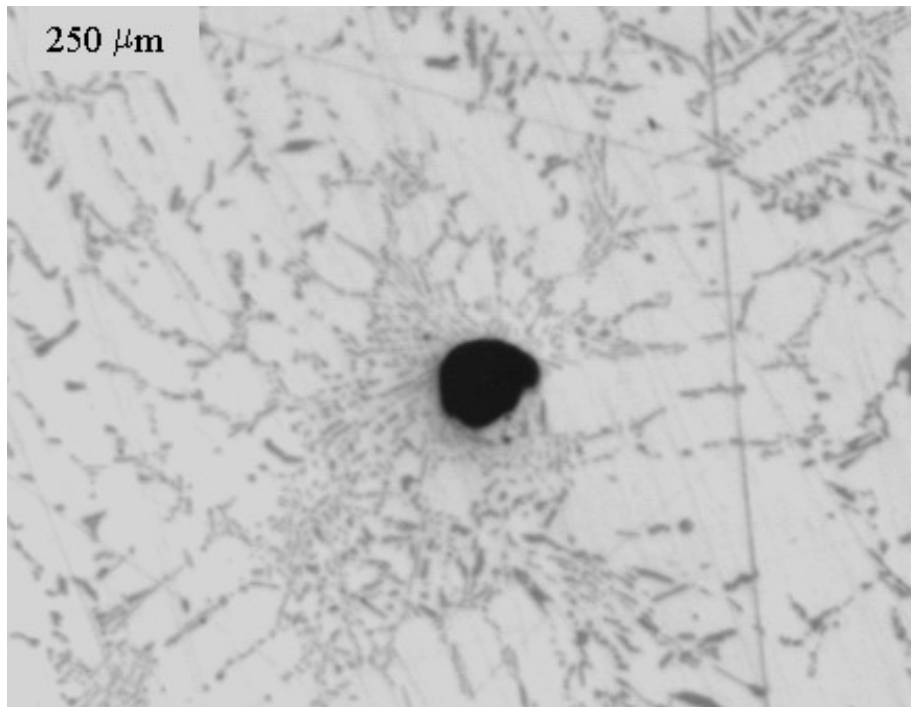
Figure 9. The measured distributions of casting defect density (number per unit area) in casting plates. (a) RR runner; (b) VR runners.



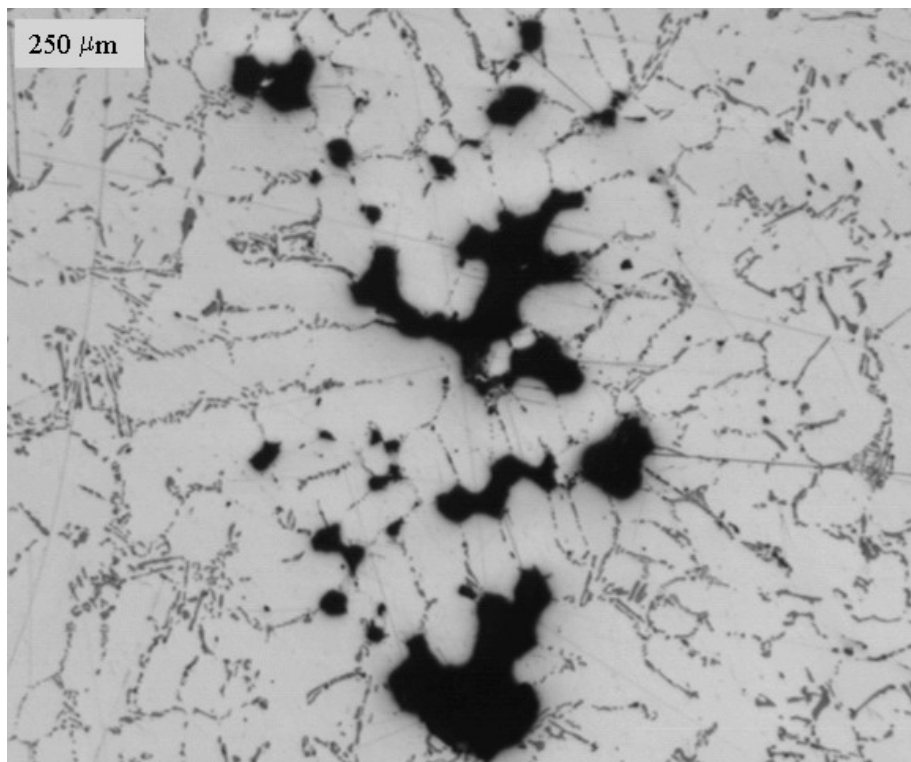
(a)

(b)

Figure 10. The measured area fraction distribution of casting defects in casting plates. (a) RR runner; and (b) VR runner.



(a)



(b)

Figure 11. Typical microstructures of various porosities in polished surfaces of the samples, acquired by using optical microscope (from Omniment3 Instrument Image Analyser). (a) Porosity (b) Shrinkage porosities.

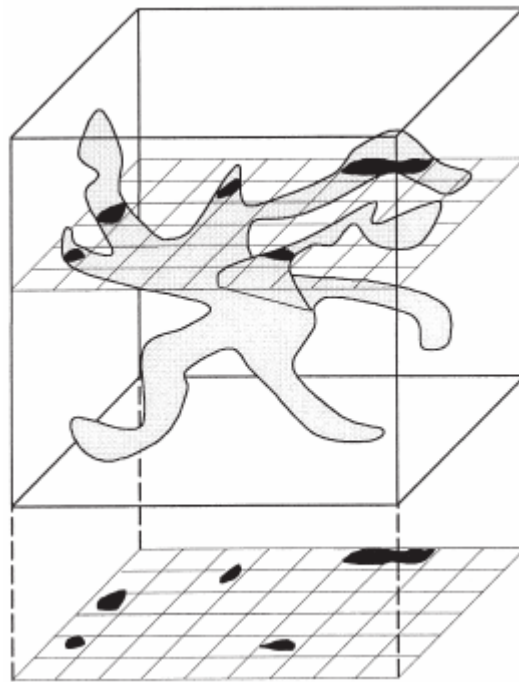


Figure 12. Schematic display of a shrinkage pore and the two-dimensional image acquired when the sample is sectioned.

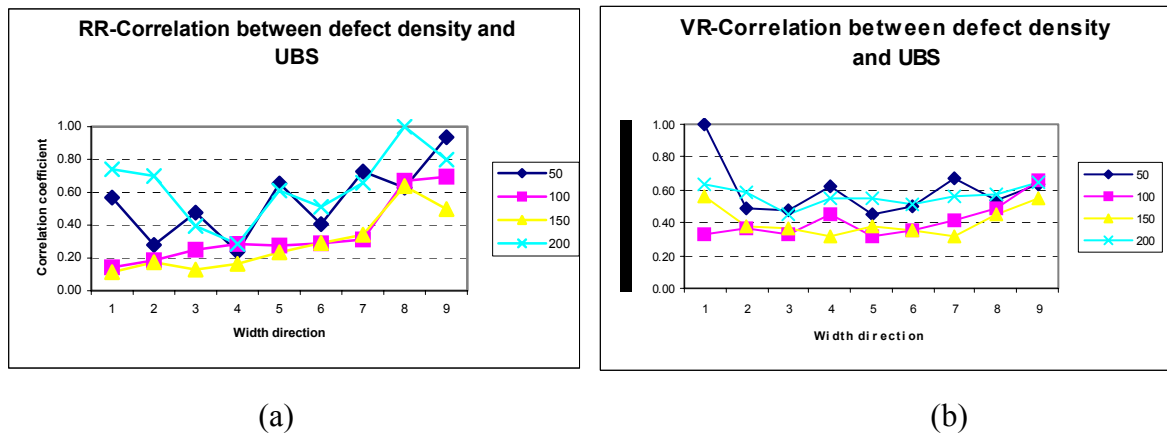


Figure 13. The correlation coefficient distribution plots between casting defect density and three-point bend strength (UBS). (a) RR runner; (b) VR runner.

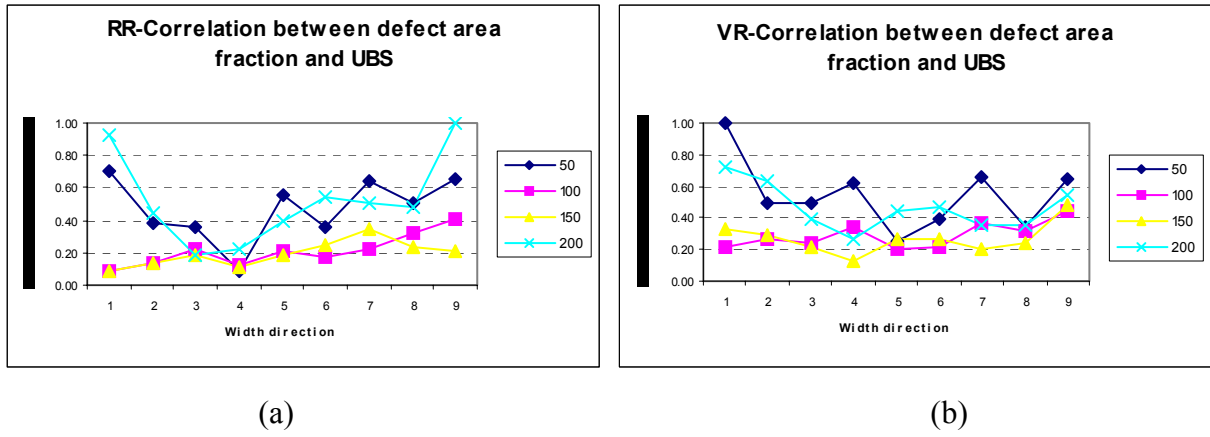


Figure 14. The correlation coefficient distribution plots between casting defect area fraction and three-point bend strength. (a) RR runner; (b) VR runner.